Article

Determination of the Local Electric Field at Au/SAM Interfaces Using the Vibrational Stark Effect

Jana K. Staffa,[†] Lisa Lorenz,[†,§] Michael Stolarski,[†] Daniel H. Murgida,[‡] Ingo Zebger,[†] Tillmann Utesch,[†] Jacek Kozuch,*[,†,‖] and Peter Hildebrandt*[,†]

[†]Institut für Chemie, Technische Universität Berlin, Sekr. PC14, Straße des 17. Juni 135, D-10623 Berlin, Germany

[‡]Universidad de Buenos Aires, Instituto de Química Física de los Materiales Medio Ambiente y Energía, Ciudad Universitaria, 1053 Buenos Aires, Argentina

Ⓢ *Supporting Information*

ABSTRACT: A comprehensive understanding of physical and chemical processes at biological membranes requires the knowledge of the interfacial electric field which is a key parameter for controlling molecular structures and reaction dynamics. An appropriate approach is based on the vibrational Stark effect (VSE) that exploits the electric-field dependent perturbation of localized vibrational modes. In this work, 6-mercaptohexanenitrile (C5CN) and 7-mercaptoheptanenitrile (C6CN) were used to form self-assembled monolayers (SAMs) on a nanostructured Au electrode as a simple mimic for biomembranes. The C≡N stretching mode was probed by surface enhanced infrared absorption (SEIRA) spectroscopy to

determine the frequency and intensity as a function of the electrode potential. The intensity variations were related to potential-dependent changes of the nitrile orientation with respect to the electric field. Supported by electrochemical impedance spectroscopy, molecular dynamics simulations, and quantum chemical calculations the frequency changes were translated into profiles of the interfacial electric field, affording field strengths up to 4×10^8 V/m (C6CN) and 1.3×10^9 V/m (C5CN) between +0.4 and −0.4 V (vs Ag/AgCl). These profiles compare very well with the predictions of a simple electrostatic model developed in this work. This model is shown to be applicable to different types of electrode/SAM systems and allows for a quick estimate of interfacial electric fields. Finally, the implications for electric-field dependent processes at biomembranes are discussed.
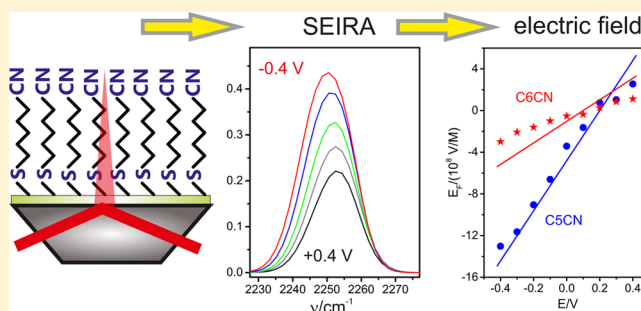
■ INTRODUCTION

Many processes at biological membranes are controlled by variations of the transmembrane potential. This is most obvious for voltage-gated ion pumps and channels for which the specific functions can readily be linked with experimentally accessible voltage changes across membranes.[1−3] The underlying molecular cause-action mechanisms are by far not fully understood, despite the progress in structural analysis. To elucidate how a change of the transmembrane potential of tens of millivolts activates the molecular machines, requires a more detailed consideration of the potential distribution across the lipid bilayer. In fact, due to the additional contributions of the surface and dipole potentials, the total potential does not vary linearly from one side of the membrane to the other.[4] Particularly, in the interfacial regions, there are sharp potential drops over short distances which correspond to high local electric fields of up to 10^9 V/m. Such high electric fields are capable of affecting molecular structures and the transfer of charges,[5−8] suggesting that the modulation of local electric fields via the transmembrane potential constitute the physical trigger for molecular changes that activate ion pumps or open ion channels. A similar mechanism may also hold for membrane-attached proteins that are assumed to function in

response to membrane potential changes. Albeit plausible, this interpretation requires further substantiation by quantifying the magnitude of the electric field strength, which in view of the complex composition of natural membranes represents a formidable challenge. In this respect, efforts were made to use membrane models that mimic essential structural and electrical features of the natural template but are easier to investigate.[9]

Convenient membrane models are based on electrodes that are coated with layers of amphiphiles, including mono- or bilayers with incorporated or peripherally bound proteins.[9−12] Here the potential at the supporting electrode is the parameter to alter the electric field across the model membrane. Studies on biomimetic membranes have indeed provided evidence for voltage-dependent processes of proteins and peptides.[13−18] Using Au or Ag as a supporting electrode, these devices offer the additional advantage of applying electrochemical and surface-sensitive spectroscopic techniques. Among them, surface enhanced Raman (SER) and surface enhanced infrared

absorption (SEIRA) spectroscopy play a particularly important role since they selectively probe immobilized molecular species and their structural response to electric field changes.[5–8,14–19]

Vibrational spectroscopic methods can also be used to quantify the field strength based on the vibrational Stark effect (VSE).[20] The VSE describes the perturbation of vibrational energy levels by the electric field according to

$$\nu = \nu_0 - \left(\Delta\vec{\mu} \cdot \vec{E}_f + \frac{1}{2} \vec{E}_f \Delta\alpha \cdot \vec{E}_f \right) \tag{1}$$

where $\Delta\vec{\mu}$ is the difference dipole moment (between the ground and excited vibrational states), $\Delta\alpha$ the difference polarizability, and ν_0 is the frequency in the absence of an external electric field $\vec{E}_f$. For electric field strengths below 10^{10} V/m, the quadratic term can be neglected,[20] and then the frequency varies linearly with the electric field according to

$$\nu \cong \nu_0 - |\nu\vec{\mu}| \cdot |\vec{E}_f| \cdot \cos\theta \tag{2}$$

where θ is the angle between vectors of the difference dipole moment and the electric field.

Widely used VSE reporter groups are nitrile functions which give rise to a characteristic IR-active mode around 2250 cm^{-1}.[20–38] This mode is an essentially pure C≡N stretching vibration such that the difference dipole moment is oriented along the bond axis pointing from the negative partial charge on the nitrogen to the positive one on the carbon atom. Unlike probes based on electronic transitions,[4] the small size of the VSE reporter group offers the advantage of mapping electric fields with a high spatial resolution in the range of molecular bond lengths and with a much lower perturbation of the system of interest. Furthermore, the C≡N stretching mode is observed in a spectral region usually free of other interfering vibrational modes. Thus, it can be detected even in biological macromolecules and has been successfully employed to determine local electrostatics in proteins and enzymes in solution and even immobilized on membrane analogues.[21,23–28,30–32,37,38]

The present work is dedicated to the electric field analysis at biomimetic membranes, focusing on self-assembled monolayers (SAMs) of amphiphiles as the simplest models for biological interfaces. We have studied SAMs of nitrile-terminated mercaptans on Au electrodes by SEIRA spectroscopy and electrochemical impedance spectroscopy (EIS), complemented by theoretical methods to determine the electric field at the SAM/solution interface as a function of the electrode potential E. The results were compared with the predictions of an electrostatic model for the interfacial potential distribution and related to earlier SER-spectroscopic results on nitrile-terminated SAMs.[33–36] Finally, we briefly discuss the implications of the present findings for the electric field control of biological processes at biomimetic and natural membranes.

■ MATERIALS AND METHODS

Materials. For the synthesis of di(6-hexanenitrile)-disulfide or di(7-heptanenitrile)-disulfide, the respective 6-bromohexanenitrile (1 equiv) or 7-bromoheptanenitrile (1 equiv) was added to a solution of borhydride exchange resin (1 equiv) and sulfur powder (1 equiv) in methanol at ambient temperature. After stirring for 10 min, the resin was filtered off and methanol was removed under reduced pressure and lyophilized to remove the water residues. The resulting oil was purified by HPLC. The purity of the products, di(6-hexanenitrile)-disulfide and di(7-heptanenitrile)-disulfide were checked by standard analytical techniques (Supporting Information). These disulfides dissociated into thiolates, which correspond to the thiol species 6-mercaptohexanenitrile (C5CN) and 7-mercaptoheptanenitrile (C6CN), upon self-assembly on the Au surface due to the formation of Au–S bonds. All chemicals used for the synthesis and for spectroscopic experiments, including *n*-mercaptobutylnitrile (C4CN) and acetonitrile (ACN), were of highest purity grade available.

Spectroscopy. Nanostructured Au films were generated by electroless deposition[39] on a trapezoidal-shaped ATR-IR silicon crystal ($W \times L \times H = 20 \times 25 \times 10$ mm^3). The SAM was formed on the Au film upon immersing the coated ATR-crystal in a 1 mM solution of the disulfides or the thiol in ethanol. SEIRA spectra were measured using a Bruker Tensor27 spectrometer or an IFS66v/s FTIR-spectrometer equipped with a MCT photoconductive detector and a Kretschmann-ATR setup adjusted to an angle of incidence of 60°. IR spectra of the nitriles in solution were measured with an ATR setup which consisted of the same homemade cell as for SEIRA measurements but lacking the Au-film on the ATR-IR silicon crystal, or with a thin-layer transmission sandwich cell using the Bruker IFS66v/s or Tensor27 FTIR-spectrometer. All spectra were recorded between 1000 and 4000 cm^{-1} with a spectral resolution of 4 cm^{-1}.

Electrochemistry. Electrochemical experiments were performed using a μAutolabII/FRA2 instrument controlled via the FRA and GPES software for EIS and cyclic voltammetry (CV). The three-electrode system consisted of the Au film as the working electrode (geometrical area 0.67 cm^2 with a roughness factor of 2.4, corresponding to a real area of 1.6 cm^2), a Pt counter electrode, and a Ag/AgCl (3 M KCl) reference electrode, to which all potentials cited in this work refer to. Potential-dependent EIS was performed from +0.4 to −0.4 V in a frequency range from 0.05 Hz to 100 kHz. CVs were measured between +0.4 and −0.4 V at scan rates of 0.2 V s^{-1}. Between these limiting potentials, the SAMs were found to be stable and thus this range was also used in all other electrochemical and spectroelectrochemical experiments, which were carried out in solutions at pH 7.0 (30 mM phosphate buffer).

Calculations. DFT calculations were carried out using the B3LYP functional. For geometry optimization, the 6-311G* basis set was used. The optimized structure was oriented with the C≡N bond along the z-axis for the optimization using the keywords "opt = tight" and "int = ultrafine" and anharmonic frequency calculation with B3LYP/6-311++G**, while applying different electric field strengths along the z-axis. To consider the effect of different solvents on the C≡N stretching frequency, the calculations of acetonitrile were carried out specifying the respective solvent permittivity within the SCRF model of Gaussian09. In this model, the solvent is described due to Onsager's reaction field theory.

All-atom molecular dynamics (MD) simulations were carried out with C5CN and C6CN SAMs on Au surfaces in aqueous solution. Each model contained 672 monomers which were covalently linked via the sulfur atoms to the Au(111) surface and the chains were initially tilted by ca. 30° with respect to the surface normal. The sulfur atoms were arranged in a $\sqrt{3} \times \sqrt{3}$ lattice on the Au surface which resulted in minimal neighboring distances corresponding to the experimentally determined value of 4.98 Å.[40] In order to maintain this coverage pattern, all sulfur and gold atoms were fixed at their positions during the
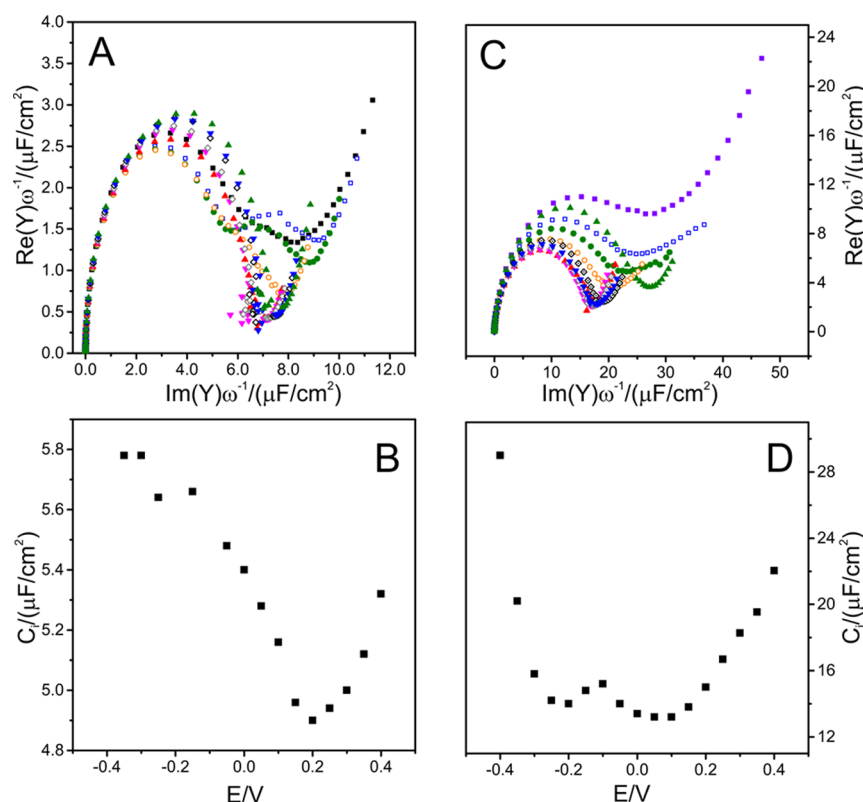
Figure 1. EIS measurements of C5CN- (A, B) and C6CN-SAMs (C, D) on nanostructured Au electrodes. Panels (A) and (C) show a selection of Cole−Cole plots at different potentials: 0.4 V (black ■), 0.3 V (blue □), 0.25 V (olive ●), 0.2 V (orange ○), 0.1 V (red ▲), 0.0 V (magenta ▼), −0.05 V (gray ◇), −0.15 V (black ◇), −0.25 V (blue ▼), −0.35 V (olive ▲). Panels (B) and (D) represent the resultant capacitance vs potential plots for C5CN and C6CN, respectively.

simulations. Au atoms were treated as uncharged and were simulated with van der Waals parameters derived by Bizzarri et al.[41] The SAM backbone was treated with the CHARMM force field for lipids,[42] and the parameters for the nitrile group were adopted from the CHARMM General force field.[43] The generated surfaces were solvated in TIP3P water boxes (ca. 120 × 120 × 110 Å^3),[44] and the experimentally used ionic strength was mimicked by addition of Na$^+$ of Cl$^-$ ions.

The subsequent all-atom MD simulations were carried out with NAMD2.10,[45] using the CHARMM force field as described above. After minimizing the energy (30 000 steps), heating to 300 K (42 ps), and thermally equilibrating the surface−solvent systems (60 ps), the models were subjected to 15 ns long production runs. During the preparation, position constraints on all heavy atoms (25 kcal·mol^{-1}·Å^{-2}) were stepwise released. The following production dynamics was carried out without constraints except for the fixed atom positions (vide supra). During the 15 ns simulation, the number of particles (N), pressure (p = 1 atm), and temperature (T = 300 K) were kept constant using Langevin piston dynamics.[46] Additionally, no volume fluctuation along the surface plane was allowed to maintain the perfect lattice of the sulfur atoms in the periodic system. Real space electrostatics and van der Waals interactions were truncated above 12 Å. Long-range electrostatics was calculated with the Particle Mesh Ewald summation.[47] The applied time step of 2 fs was allowed by restraining all bonds including hydrogen with the SHAKE algorithm.[48]

For analyzing the geometric properties of the SAMs and the resulting hydrogen bonds between the nitrile label and water

molecules, VMD1.8.6 was used.[49] Hydrogen bonds were defined by the criteria that the donor−acceptor distance was smaller than 3.5 Å and the donor−hydrogen−acceptor angle smaller than 30°.

■ RESULTS

Electrochemical Measurements. Potential-dependent EIS measurements were performed between +0.4 V and −0.4 V. Cole−Cole plots were obtained by taking into account the effective Au surface area of 1.6 cm^2 (Figure 1A, C). To exclude effects based on model-dependent fitting, the potential-dependent interfacial capacitance C_I was obtained graphically from the radii of the semicircles, multiplied by a factor two (Figure 1B, D).[50,17] Depending on the quality of the SAM and the surface area, the capacitance varies for different measurements of the same type monolayer (see Supporting Information, Figure S1). This is reflected by the C_I values which, at the minima of the $C_i = f(E)$ curves, were found between 5 and 8 $\mu F/cm^2$ and between 5 and 13 $\mu F/cm^2$ for C5CN and C6CN, respectively. The values are within the range of previously reported data.[51,52]

IR Spectroscopic Experiments. Several methods have been used to determine the difference dipole moment (Stark tuning rate).[20] One experimental approach employed also in this work is based on Onsager's reaction field theory. Accordingly, the solute occupies a spherical cavity inside a continuous dielectric medium represented by the solvent. The average electric field $\vec{F}_{ons}$ (in SI units) created by a solvent can be calculated as a function of solute and solvent properties according to

$$\vec{F}_{ons} = \frac{\mu_0}{3\epsilon_0} \frac{\rho}{M} N_a \frac{2(\epsilon - 1)}{2\epsilon + n^2} \frac{n^2 + 2}{3} \qquad (3)$$

where N_a, ε_0, ρ, and M are the Avogadro number, the permittivity in vacuo, the density of the solute, and its molecular weight, respectively. The static dielectric constant (ε) describes the capacity of the solvent to be polarized and the refractive index (n) represents the capacity to polarize its environment (see Supporting Information, Table S1). The property of the solute is considered via the gas-phase dipole moment in the ground state (μ_0). Using eq 3, the reaction fields can be calculated for different solvents, which were used for IR measurements of the C≡N stretching frequency. For these experiments, we have employed acetonitrile (ACN) due to its solubility in a large range of solvents, in contrast to C5CN and C6CN. As expected from eq 3, the frequencies follow the reaction field strength in an approximately linear behavior with a slope of 1.3×10^{-9} cm^{-1}/(V·m^{-1}) that corresponds to the modulus of the Stark tuning rate (Figure 2B). This is true for
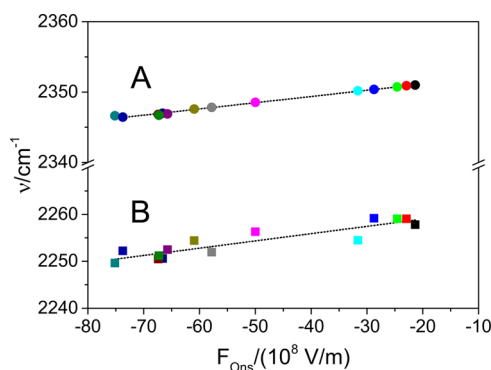

Figure 2. Dependence of the C≡N stretching frequency of acetonitrile on the average reaction field F_{ons} provided by different solvents as determined by eq 3. (A) Frequencies obtained from DFT calculations; (B) experimentally determined frequencies from IR measurements. The data points from left to right refer to isopentane, *n*-hexane, *n*-heptane, cyclohexane, tetrachlormethane, tetrahydrofuran, dichlormethane, propanol, acetone, ethanol, methanol, dimethyl sulfoxide, and propylene carbonate. The frequencies determined in solutions of the three alcohols were corrected for the hydrogen bonding effects by −8.5 cm^{-1} (see text and Supporting Information for further details).

solvents that have no hydrogen-bonding capacities. In fact, such specific interactions exert a strong influence on the C≡N stretching frequency, which is known to be larger than the VSE itself.[20,26,53,54] To determine this effect quantitatively, we have measured the spectra of ACN and *n*-mercaptobutylnitrile (C4CN) in aqueous buffer solution (pH 7.0, as used for SEIRA experiments, vide infra).

Comparing the frequencies with those determined in propylene carbonate, which exhibits a very similar albeit not identical reaction field as water according to eq 3, we note an upshift from propylene carbonate to H$_2$O by 7.8 and 8.3 cm^{-1} for ACN and C4CN, respectively (Figure 3). Using the fit of eq 3 to the experimental data in Figure 2B, the expected C≡N frequency for the reaction field of water is 2251.2 cm^{-1} (based on the Onsager model in absence of hydrogen bonds), corresponding to a frequency difference of 8.9 cm^{-1} compared to the experimental value in aqueous solution.

Thus, we conclude that for both ACN and C4CN the frequency upshift due to hydrogen bonding interactions is ca.
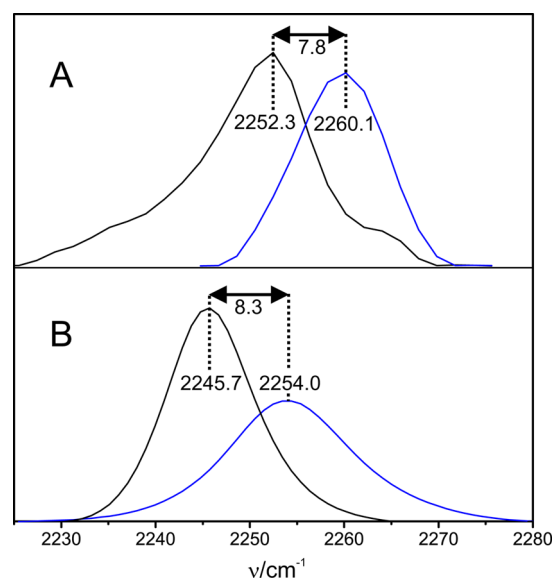

Figure 3. Nitrile stretching modes of (A) ACN and (B) C4CN in propylene carbonate (black trace) and aqueous solution (blue trace, buffered to pH 7.0).

8.5 cm^{-1} in average. Indeed, after correction by this quantity, also the frequencies of ACN in methanol, ethanol, and propanol follow the linear relationship in Figure 2B. Similar hydrogen-bonding induced frequency upshifts have also been determined for other nitrile compounds indicating that hydrogen bonding effects are localized on the nitrile function and represent an incremental contribution to the total frequency shift.[20,26,53,54] Furthermore, previous results also indicated that the Stark tuning rates for H-bonded and non-H-bonded nitriles display similar values.[26] Note that the bandwidth (fwhm) of C4CN (but not of ACN) is significantly increased in H$_2$O (15 cm^{-1}) compared to PC (10 cm^{-1}) (Figure 3). Such an effect was described before and attributed to different interactions of the nitrile group with the solvent, either via the π-orbital or the p-orbital on the nitrogen,[55] or due to different angles of the H-bond in respect to the C≡N axis.

Density Functional Theory Calculations. DFT calculations were carried out in two directions. First, the C≡N stretching frequency was calculated for ACN in different solvents using the implicit solvent model provided by Gaussian09. These data afford a slope of 0.9×10^{-9} cm^{-1}/(V·m^{-1}) (Figure 2A) which is smaller by a factor of 1.3 than the Stark tuning rate derived from the experimental data (Figure 2B). Note that the calculated C≡N stretching frequencies are distinctly higher than the experimental frequencies due to the intrinsic errors of the DFT calculations. However, these errors are systematic such that their effect on the reaction field dependence can be neglected. Second, DFT calculations were carried out for C5CN and C6CN in vacuo by employing external electric fields. Here the optimized structures were oriented to bring the nitrile bond axis parallel to the direction of the electric field. This configuration served as the starting point for the calculation of the anharmonic C≡N stretching frequencies. Figure 4 shows a decrease of the stretching frequencies with increasing electric field strength which can be described by a linear function. For both C5CN and C6CN, the slope of the function, i.e., the Stark tuning rate, is determined to be 3.9×10^{-9} cm^{-1}/(V·m^{-1}).
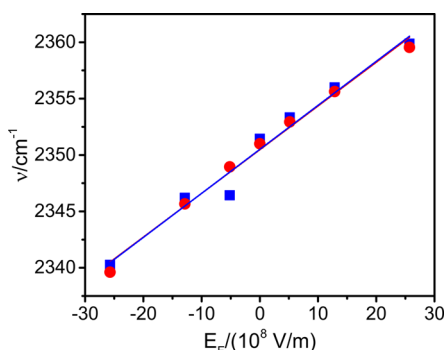
Figure 4. Calculated nitrile stretching frequencies of C5CN (blue) and C6CN (red) as the function of the electric field E_F. The DFT calculations refer to the molecules in vacuo and the external electric field was oriented along the C≡N bond. The solid line represents the least-squares fit to all calculated frequencies.

SEIRA Experiments. Potential-dependent SEIRA measurements were performed starting at +0.4 V and then decreasing the potential in steps of 0.1 to −0.4 V (Figure 5).
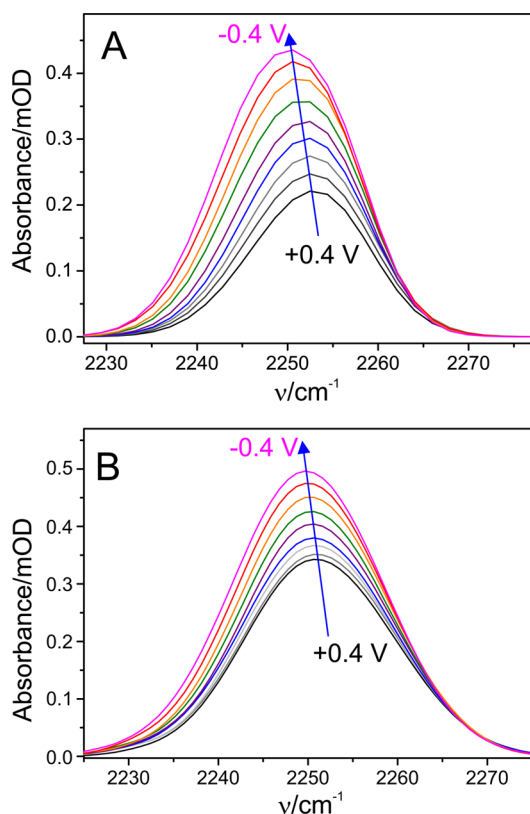

Figure 5. Potential-dependent SEIRA spectra in the C≡N stretching region of (A) C5CN and (B) C6CN SAMs on an Au electrode.

For both C5CN and C6CN, the frequencies decrease with decreasing potential concomitant with an increase of the band intensity. These potential-dependent spectral changes were found to be fully reversible and experiments with different electrode preparations afforded the same results within the experimental accuracy, demonstrating the high reproducibility of the SEIRA experiments. The spectra were analyzed by fitting Gaussian functions to the experimentally observed bands. It turned out that despite the slightly asymmetric band shape a single Gaussian function provided a satisfactory fit that was not significantly improved by including further Gaussian functions. The results of spectra analysis are shown in Figure 6. The data reveal a linear potential-dependence of the SEIRA intensity whereas the potential-dependent frequency changes follow a nonlinear behavior.

Molecular Dynamics Simulations. For both C5CN and C6CN SAMs the model comprised 672 monomers attached to the surface in a regular array. After equilibration, the average angles φ between the C≡N bond axes and the surface normal were determined for each monomer during entire simulation period of 15 ns. The resulting angles were averaged over all monomers leading to ca. 68° and 63° for C5CN and C6CN, respectively (Figure 7A).

As a control, we also determined the average angles for the last 5 ns simulation which afforded same results. For C5CN, the simulations demonstrated a narrow distribution with a sharp maximum, indicating a homogeneous and stable configuration of the SAM on the surface. In contrast, the distribution for C6CN was much broader, independent of the time window of the simulation, including a substantial fraction of monomers with C≡N inclination angles smaller than 63°. The different orientational flexibilities of the nitrile functions in C5CN and C6CN are accompanied by different hydrogen bonding contacts with water molecules, setting the limits for hydrogen bonding to a distance of 3.5 Å to the nitrile nitrogen and an angle (C≡N−H−OH) of 30°. Thus, one obtains, on the average, 0.57 and 0.63 hydrogen bonds per SAM molecule for C5CN and C6CN, respectively (Figure 7B). These values have to be compared to the respective monomers in solution for which a value of 0.94 was determined.

■ **DISCUSSION**

To translate the frequency shifts into local electric fields according to eq 2, we need to know the C≡N stretching frequency at zero electric field (ν_0), the Stark tuning rate $|\Delta\vec{\mu}|$, and the angle θ between the difference dipole moment of the nitrile function and the electric field. Here, ν_0 can be set equal to the frequency at $E_{pzc,eff}$, i.e., the electrode potential at which the electric field at the SAM/solution interface is zero.

Effective Potential of Zero Charge. The potential-dependence of the interfacial capacitance, as derived from the EIS experiments (Figure 1), allows for determining the effective potential of zero charge, corresponding to the potential of minimum capacitance.[56] The shape of these curves varied somewhat from measurement to measurement as has been noted by Becka and Miller.[56] These authors attributed the limited reproducibility mainly to the incorporation of impurities and ions into the SAM. Such effects may be particularly relevant when, concomitant to inevitable differences of the (sub)-nanoscopic roughness of the electrode surface in the individual experiments, the amount of defects of the SAM is altered. However, despite these variations, a single minimum at ca. +(0.2 ± 0.05) V was identified for C5CN SAMs. In contrast, the C6CN SAMs afforded two usually poorly defined minima at ca. +0.1 and −0.2 V. Thus, we conclude that the double-well shape of the capacitance curve is mainly related to the specific properties of the C6CN SAM. In fact, MD simulations indicated a distinct difference between C5CN and C6CN SAMs. Whereas the C5CN SAM adopted a highly homogeneous structure as reflected by the narrow distribution of the nitrile tilt angle with respect to the surface normal (68° with $\Delta\varphi \cong 10°$; Figure 7A), the much broader distribution for the
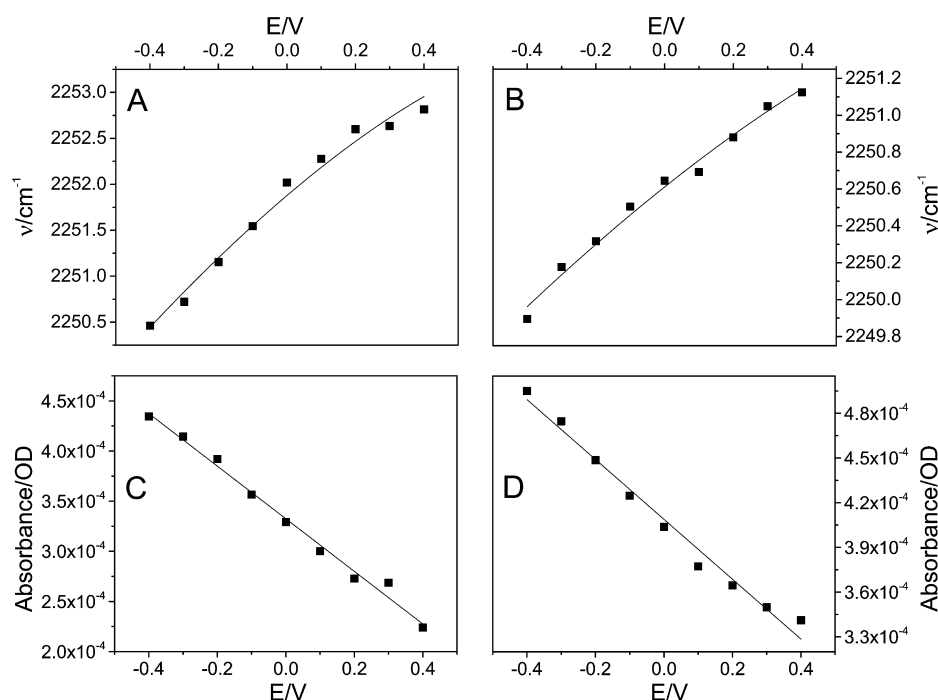
Figure 6. Potential-dependent changes of the frequencies (top) and intensities (bottom) of (A, C) C5CN and (B, D) C6CN SAMs derived from the SEIRA measurements (Figure 5). The solid lines represent linear and nonlinear fits to the experimental intensity and frequency data, respectively, as described in the Discussion section.
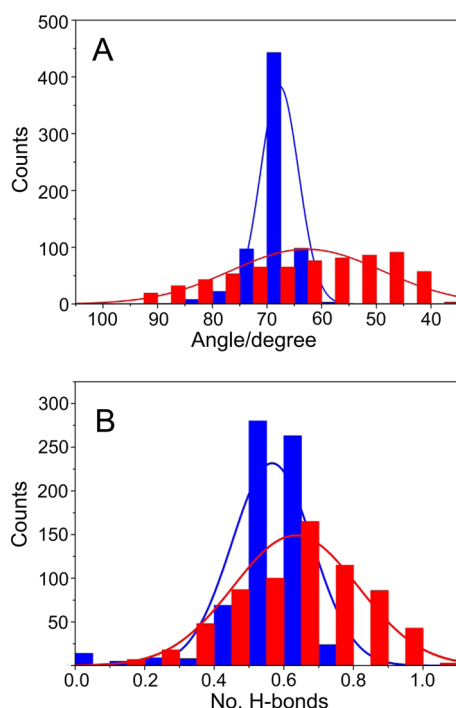

Figure 7. Distribution of (A) the tilt angle φ of the C≡N bond with respect to the surface normal and (B) the number of hydrogen bonding contacts as derived from the MD simulations. The blue and red data refer to C5CN and C6CN, respectively.

C6CN SAM ($\Delta\varphi > 35°$; Figure 7A) points to a substantial structural heterogeneity, which may be further enhanced by the nanostructured morphology of the Au support. The broader distribution of the tilt angle φ is also consistent with the larger bandwidth of the C≡N stretching for C6CN than for C5CN (20 vs 16 cm^{-1}; Figure 5).

For a qualitative discussion of the effective potential of zero charge we consider the incremental contribution of the SAM and the SAM/solution interface $\Delta\Phi_{SAM}$ to $E_{pzc,eff}$ according to

$$E_{\text{pzc,eff}} = E_{\text{pzc}} + \Delta\Phi_{SAM} \qquad (4)$$

where E_{pzc} is the potential of zero charge of the bare polycrystalline Au, for which a value of +0.06 V was determined.[57] For methyl-terminated SAMs, the quantity $\Delta\Phi_{SAM}$ is mainly controlled by the dipole moment contribution of the alkylthiol that may be approximated by the dipole moment of the respective neutral radical thiol.[58] The direction of this dipole moment points from the Au surface to the solution. Its modulus was calculated to increase with increasing chain length, which thereby results in an increasing negative shift of $E_{pzc,eff}$ ($\Delta\Phi_{SAM} < 0$).[59] On the basis of this data and assuming that this tendency also holds for nitrile-terminated SAMs, one would estimate that $E_{pzc,eff}$ of Au/C6CN is more negative by 0.1 V than Au/C5CN solely due to the longer alkyl chain. However, the polar nitrile group provides an additional contribution to the overall dipole moment of opposite sign such that $\Delta\Phi_{SAM}$ may become positive and thus affords an upshift of $E_{pzc,eff}$ compared to E_{pzc} for both C5CN and C6CN.[54,60] Consequently, one can rationalize the $E_{pzc,eff}$ value of +0.2 V for Au/C5CN. Taking into account the chain-length dependent decrease of $\Delta\Phi_{SAM}$ by 0.1 V one would therefore expect $E_{pzc,eff} \approx + 0.1$ V for Au/C6CN which in fact corresponds to the faint capacitance minimum at more positive potentials (Figure 1D). According to this interpretation, the contribution of the nitrile function to the overall dipole moment of the SAM should depend on the tilt angle φ. Therefore, the second minimum at more negative potentials in Figure 1D is tentatively attributed to a domain of the C6CN SAM that is characterized by larger tilt angles (see Figure 7A) and thus negligible contributions of its dipole moment to $\Delta\Phi_{SAM}$, resulting in a net downshift of $E_{pzc,eff}$ compared to E_{pzc}.

This latter population of the C6CN SAM, however, would hardly be detectable in the SEIRA experiments since the surface enhancement of the C≡N stretching mode scales with $(\cos \varphi)^2$ (vide infra).[61] Consequently, for the following analysis of the SEIRA spectra, we will assume $E_{pzc,eff}$ to be +0.2 and +0.1 V for C5CN and C6CN, respectively.

To our knowledge, there is only one published study on the potential of zero charge of polycrystalline Au coated by SAMs of nitrile-terminated alkylthiols.[62] Using the electrowetting technique, these authors reported a value of ca. + 0.24 V for C11CN that falls in the range of those determined in this work (vide supra). This concordance lends further credence to the present results and supports the applicability of the EIS approach for $E_{pzc,eff}$ determination. Note that also for methyl-terminated SAMs different techniques (immersion technique, electrowetting, and differential capacitance measurements) provided a similar agreement (e.g., ca. − 0.4 ± 0.1 V for C11CH₃), whereas significant deviations are noted when the same methods were applied to hydroxyl-terminated SAMs ($\Delta E_{pzc,eff} \approx 0.5$ V).[56,58,62,63] Possibly, the $E_{pzc,eff}$ determination depends more sensitively on the method if the terminal functions have hydrogen-bond donor properties.

The Nitrile Stretching Frequency at $|\vec{E}_f| = 0$. The frequencies at zero electric field refer to the frequencies at $E_{pzc,eff}$ and thus can be obtained from frequency-potential plots (Figure 6A,B), affording 2252.5 and 2250.8 cm^{-1} for C5CN and C6CN, respectively. The different values for ν_0 can be rationalized in terms of "odd−even" and hydrogen bonding effects. First, according to previous data on alkylnitriles,[64] the intrinsic nitrile stretching frequency in aprotic solvents of C6CN monomers is expected to be lower by ca. 4 cm^{-1} than that of C5CN. This difference is two times larger than that of the experimentally determined ν_0 values (1.7 cm^{-1}). However, hydrogen-bonding interactions, which cause an upshift of the C≡N stretching frequency, are different for C6CN than for C5CN. Taking the average contacts of the nitrile function with water molecules as a measure for the strength of hydrogen bonding interactions, one would expect a larger hydrogen-bond induced frequency upshift for C6CN SAMs (Figure 7B), such that the different zero-field frequencies can readily be understood.

Stark Tuning Rate. The Stark tuning rate can be obtained using various techniques,[20] i.e., using vibrational Stark spectroscopy (VSS) in a frozen glass, solvatochromic IR measurements, or quantum chemical calculations. Each method is associated with intrinsic limitations. While VSS represents the most direct measurement, the result, $|\Delta\vec{\mu}|\cdot f$, contains the local field factor f, which is assumed to be $f \approx 1.5$−2.5.[20,65] For the nitrile function, $|\Delta\vec{\mu}|\cdot f$ was determined to be 4.3×10^{-9} cm^{-1}/(V·m^{-1}), or $|\Delta\vec{\mu}| \approx (2.3 \pm 0.6) \times 10^{-9}$ cm^{-1}/(V·m^{-1}) after correction for f.[66] In this work, we have determined the Stark tuning rate $|\Delta\vec{\mu}|$ experimentally by solvatochromism analysis and DFT calculations. Both methods provide a direct measure for $|\Delta\vec{\mu}|$, but also suffer from considerable pitfalls as recently discussed by Fried and Boxer.[20] The value obtained by DFT calculations is assumed to be overestimated by ca. 25%. Accordingly, the "real" value would be ca. 3×10^{-9} cm^{-1}/(V·m^{-1}) instead of 3.9×10^{-9} cm^{-1}/(V·m^{-1}) which is in good agreement with the value determined for ACN by first-principle methodology.[67]

The Stark tuning rate derived from the solvatochromism analysis using Onsager theory (Figure 2B) is also assumed to be slightly overestimated due to the neglect of higher order (polarizability) effects.[20] However, at the same time, further underlying assumptions of the Onsager eq (eq 3) may be questioned, such as the "spherical cavity" assumption and the lack of specific solute−solvent interactions. Deviations from the spherical shape of the cavity, for instance, may instead lead to an underestimation of the resultant Stark tuning rate. This becomes apparent in the case of benzonitrile, where solvatochromism yielded a Stark tuning rate of 1.43×10^{-9} cm^{-1}/(V·m^{-1}) (after correction for the missing factor of $4\pi/3$ in the Onsager equation in ref 22; see also ref 20), but the value obtained from VSS yielded $|\Delta\vec{\mu}| \approx 3.2 \times 10^{-9}$ cm^{-1}/(V·m^{-1}) based on $|\Delta\vec{\mu}|\cdot f = 6 \times 10^{-9}$ cm^{-1}/(V·m^{-1}). A similar underestimation by a factor of ca. 2 (±0.9; based on the fields calculated for DMSO) results also for different carbonyls when comparing results from VSS and solvatochromism.[65] Thus, multiplying this factor of ca. 2 to the value of 1.3×10^{-9} cm^{-1}/(V·m^{-1}) determined for acetonitrile from solvatochromism and Onsager theory in this work, we obtain a corrected value of ca. 2.6×10^{-9} cm^{-1}/(V·m^{-1}). The same uncertainties hold when employing the Onsager equation on the basis of DFT-calculated frequencies, together with the polarizable continuum model (Figure 2A). Here, an even lower Stark tuning rate is obtained, i.e., 0.9×10^{-9} cm^{-1}/(V·m^{-1}), which again may need to be corrected by the same factor of ca. 2 to result in 1.8×10^{-9} cm^{-1}/(V·m^{-1}).

All of the corrected values for the Stark tuning rate are close or within the limits of the value obtained by VSS, i.e., $|\Delta\vec{\mu}| \approx (2.3 \pm 0.6)\cdot10^{-9}$ cm^{-1}/(V·m^{-1}). Thus, for the following analysis, we will use the ("corrected") DFT-calculated value of 3.0×10^{-9} cm^{-1}/(V·m^{-1}), which represents the upper limit for the Stark tuning rate of aliphatic nitriles, so that in turn the resultant calculated electric fields in this work represent a lower limit.

Potential-Dependence of the SEIRA Intensities. The SEIRA intensity varies linearly with the electrode potential (Figure 6C,D). Since the surface enhancement of the IR absorption scales with $(\cos \varphi)^2$,[61] i.e.,

$$I_{SEIRA} = B_s(\cos(\varphi))^2 \tag{5}$$

with B_s being a proportionality constant, this variation is likely to reflect the potential-dependence of the tilt angle φ which one may approximate by a linear function

$$[\cos(\varphi(E))]^2 = [\cos(\varphi_0)]^2 + b(E - E_{pzc,eff}) \tag{6}$$

with φ_0 as the tilt angle at $E_{pzc,eff}$ and b a proportionality constant. Combining eqs 5 and 6 leads to

$$I_{SEIRA} = B_s[\cos(\varphi)_0]^2 + B_s b(E - E_{pzc,eff}) \tag{7}$$

The average tilt angles determined by MD simulations refer to the case of zero electric field and hence correspond to φ_0. Using these values, linear fits to the intensity vs potential plots in Figure 6C,D can then be used to determine the constants B_s and b (Supporting Information, Table S2). For both SAMs, one obtains very similar results for the potential-dependent orientation of the nitrile function with b equal to ca. −0.12 V^{-1}.

Potential-Dependence of the Nitrile Stretching Frequency. To analyze the potential-dependent frequency changes in the SEIRA experiments (Figure 6A,B), we need to relate the electrode potential with the local electric field E_F at the position of the nitrile functions, i.e., at the SAM/solution interface. This correlation is based on a description of the potential drops across the electrode/SAM/solution interfaces,

originally designed by Smith and White,[68] and later further expanded in our group.[69,54] In the present work, we extend this model to account for the different polarities of the alkyl chains of the SAM and the headgroup region to describe the electric field at the CN group more accurately and obtain (see the Supporting Information)

$$E_F = \frac{\varepsilon_0 \varepsilon_S \kappa - k}{\varepsilon_0 \left[\frac{\varepsilon_1 \varepsilon_2 (d_1 + d_2)}{d_1 \varepsilon_2 + d_2 \varepsilon_1} + \varepsilon_S \kappa (d_1 + d_2) \right]} (E - E_{pzc,eff}) \quad (8)$$

where ε_1, ε_2, and ε_S are the dielectric constants of the alkyl chains, the headgroup region, and the solution, ε_0 denotes the permittivity, d_1 and d_2 are the thicknesses of the two SAM regions, and κ the reciprocal Debye length of the diffuse double layer at the SAM/solution interface. The parameter k describes the assumed linear potential-dependence of the charge density in the outer Helmholtz layer of the SAM/solution interface. According to eq 8, this electrostatic model predicts a linear relationship between the electric field experienced by the nitrile functions and the electrode potential. As discussed in detail in the Supporting Information, one may substitute θ in eq 2 by the angle between $\Delta\vec{\mu}$ and the surface normal φ. Then $|\vec{E_F}|$ can be expressed by eq 8 to obtain

$$\nu = \nu_0 + \cos(\varphi)|\Delta\vec{\mu}| \frac{\varepsilon_0 \varepsilon_S \kappa - k}{\varepsilon_0 \left[\frac{\varepsilon_1 \varepsilon_2 (d_1 + d_2)}{d_1 \varepsilon_2 + d_2 \varepsilon_1} + \varepsilon_S \kappa (d_1 + d_2) \right]} (E - E_{pzc,eff}) \quad (9)$$

This relationship implies that the electric field vector is (anti)parallel to the surface normal and its direction is given by $(E - E_{pzc,eff})$. Since φ is a function of E, we substitute $\cos(\varphi)$ by eq 6:

$$\nu = \nu_0 + |\Delta\vec{\mu}| \frac{\varepsilon_0 \varepsilon_S \kappa - k}{\varepsilon_0 \left[\frac{\varepsilon_1 \varepsilon_2 (d_1 + d_2)}{d_1 \varepsilon_2 + d_2 \varepsilon_1} + \varepsilon_S \kappa (d_1 + d_2) \right]}$$
$$\times \left| \sqrt{[\cos(\varphi_0)]^2 + b(E - E_{pzc,eff})} \right| (E - E_{pzc,eff}) \quad (10)$$

Equation 10 provides a very good description of potential-dependence of the frequencies for both C5CN and C6CN (Figure 6A,B).

Relationship between the Interfacial Electric Field and the Electrode Potential. The changes of the nitrile stretching frequencies measured in the potential-dependent SEIRA experiments can now be used to determine the relationship between the electrode potential and the electric field in the SAM/solution interface experienced by the nitrile function. Here we first use eq 2 after substitution $\cos(\varphi)$ by eq 6 (vide supra; Supporting Information) as determined from the potential-dependence of the SEIRA intensities, i.e.,

$$E_F = -\frac{\nu - \nu_0}{|\Delta\vec{\mu}| \cdot \left| \sqrt{(\cos\theta_0)^2 + b(E - E_{pzc,eff})} \right|} \quad (11)$$

In Figure 8, these data are compared with the linear relationship between the electric field strength and the electrode potential as calculated by the electrostatic model (eq 8). In general, the model provides a very good description of the experimentally determined electric field strengths.

Only for large differences of the electrode potential with respect to $E_{pzc,eff}$, i.e., $|E - E_{pzc,eff}|$, we note more substantial deviations, specifically for C6CN. These deviations can hardly
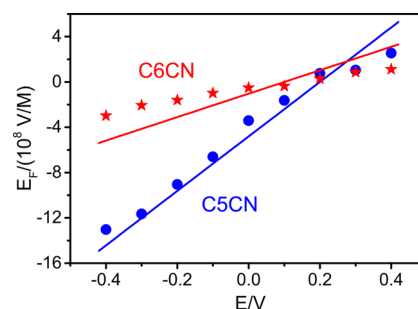

Figure 8. Variation of the electric field at the SAM/solution interface with the electrode potential for C5CN (blue) and C6CN SAMs (red). The symbols refer to the values directly obtained from the frequency shifts of the C≡N stretching using eq 11. The solid lines were obtained via eq 8.

be attributed to the neglect of the difference polarizability (quadratic term in eq 1) since this term is negligible at field strengths up to $|E_F| \approx 2 \times 10^9$ V/m.[28] Instead, they are likely to reflect the simplifications of the electrostatic model, particularly the assumed linear potential-dependence of the charge density σ_C on the SAM. This quantity refers to the effective charge distribution in the outer Helmholtz layer of the SAM layer and includes contributions of the dipoles of water molecules and the charges of ions in the first molecular layer adjacent to the nitrile function.

As shown in the Supporting Information, the values derived for σ_0 ($E = E_{pzc,eff}$) from the electrostatic model can be expressed in terms of elementary charge units per area occupied by a nitrile monomer (σ_{CN}), yielding 0.1 and 0.03 for C5CN and C6CN, respectively. These values reflect the charge needed to compensate for the effective dipole moment of the SAM and are in line with the different homogeneity of the orientation of CN head groups for both SAMs (Figure 7A). Accordingly, for C5CN, the homogeneous orientation of CN groups leads to a strong net dipole moment associated with a pronounced attraction of ions and oriented water dipoles whereas, for C6CN, the broad distribution of CN orientations leads to a diminished total dipole moment and lower accumulation of opposite charges. This renders the C6CN SAM surface more hydrophobic and may account for the considerable difference of $E_{pzc,eff}$ compared to C5CN that is larger than expected solely based on the longer chain length.[58] Furthermore, the slope $|k|$ derived from the electrostatic model, may be interpreted as the local capacitance of the headgroup region, which is estimated to be ca. 1.4 CV^{-1} m^{-1} for a high polarity ($\varepsilon \approx 78$; see the Supporting Information). Thus, the value of $|k| = 1.27$ CV^{-1} m^{-1} determined for C5CN demonstrates the highly polar character of this SAM, whereas C6CN ($|k| = 0.34$ CV^{-1} m^{-1}) displays a more hydrophobic character due to the heterogeneous distribution of CN orientations, as described above. In addition, this result demonstrates that it is possible to estimate the capacitance of a SAM headgroup region using the present approach, while it is masked in conventional electrochemical experiments due to the low capacitance of the alkyl chains ($C_{tot}^{-1} = C_1^{-1} + C_2^{-1} \approx C_1^{-1}$, with "1" and "2" referring to the alkyl chains and headgroup region).

Altogether, the simplicity of the present electrostatic model allows for a quick and semiquantitative estimate of the potential-dependence of the interfacial electric field strength in the potential range that is relevant in many electrochemical experiments, particularly in bioelectrochemistry.

General Applicability of the Electrostatic Model. It is now interesting to compare the present results with previous studies on nitrile-terminated SAMs assembled on Ag electrodes.[33−35] Oklejas et al. employed mixed monolayers of methyl- and nitrile-terminated alkanethiols (CxCH$_3$, CyCN, with x and y indicating the number of methylene groups) on nanostructured Ag, using surface enhanced Raman spectroscopy to probe the nitrile stretching frequency.[33−35] Upon varying y while keeping x constant, the nitrile group was placed at different positions in the double layer of the SAM/solution interface. For x = 10 (C10CH$_3$) and y = 11 (C11CN) the lengths of both thiols are similar and the nitrile group is located in the inner Helmholtz layer.[34] This case is most closely related to the pure C5CN and C6CN SAMs of our study.

Applying the present electrostatic model to the data of that study, one has to take into account the distinctly more negative value of E_{pzc} for Ag (−0.92 V).[57,70] As for Au, coating by nitrile-terminated SAMs is expected to shift the potential of zero charge to more positive values (eq 4). However, this effect is likely to be relatively small in view of the chain length dependence of $\Delta\Phi_{SAM}$ (vide supra),[58] such that we estimate $E_{pze,eff}$ to be ca. −0.85 V. On the basis of the approximately linear potential-dependence of the nitrile stretching frequency of C11CN/C10CH$_3$ on Ag (Figure S4),[34] ν_0 is estimated to be ca. 2250.5 cm^{-1} which is in the range of the values for C5CN and C6CN on Au determined in this work. The negative value for $E_{pzc,eff}$ implies that, in the potential range studied by Oklejas et al.,[34] E_F is positive (eq 8) and the electric field points away from the electrode toward the solution, in contrast to the opposite direction of the electric field for SAM-coated Au electrodes in the same potential range. The angle φ at Ag electrodes is estimated to be ca. 45° by taking into account the intrinsically smaller tilt angle of the methylene chain for alkyl thiols on Ag compared to Au (Supporting Information).[71] With these data, the present electrostatic model provides a consistent description for the potential-dependence of the interfacial electric field at SAM-coated Ag electrodes (see the Supporting Information for further details). Furthermore, the modulus of the electric field at the Ag/C11CN/C10CH$_3$ interface is then calculated to increase from 2.4 × 10^8 V/m at −0.8 V to 2.1 × 10^9 V/m at −0.2 V.

In this context it is important to refer to recent SER spectroscopic study on mercaptobenzonitrile SAMs on nanostructured Ag.[36] In that work, the authors demonstrated that the plasmonically enhanced radiation field at the nanostructured surface may lead to a static electric field component that may add to the interfacial electric field.[36,72] However, the photon flux used in the experiments of Oklejas et al.[33−35] was sufficiently low such that their observed frequency shifts reflect solely the unperturbed ("dark") interfacial field.

Implications for Electric Field Effects at Biological Interfaces. SAM-coated electrodes are widely employed as the simplest biomimetic membrane models as far as the simulation of the interfacial electrostatics concerned.[73] SAMs with a terminating COOH function have been used to electrostatically bind cationic proteins such as cytochrome c, the benchmark protein in bioelectrochemistry.[74] At pH values around 7.0, carboxyl-terminated SAMs are partially negatively charged (pK$_a$ = 8.2),[66] which for a mercaptoundecanoic acid (MUA) SAM is reflected by $E_{pzc,eff}$ of ca. −0.45 and −0.03 V for Ag and Au electrodes, respectively.[58,75] In an earlier study, a crude estimate, which did not consider the direction of the electric field, afforded a magnitude for the field strength of ca. 1.5 × 10^9

V/m for MUA on nanostructured Ag at E = 0.0 V, corresponding to $\Delta E = E - E_{pzc,eff} \cong 0.45$ V.[69] Nearly the same value (1.4 × 10^9 V/m) is obtained from the present reanalysis of the SERS data on C11CN/C10CH$_3$ (similar SAM thickness),[34] using the same ΔE. Thus, it seems to be that, at least under conditions when only a minor fraction of the carboxyl functions is deprotonated (ca. 6% at pH 7.0),[69] the ΔE-dependent interfacial electric field profile of carboxyl-terminated SAMs on Ag is similar to that of nitrile-terminated SAMs. If this conclusion also holds for Au electrodes, the electric field strength for SAMs of mercaptohexanoic acid (MHA) should be comparable to C5CN ($d_c \cong 10$ Å), for which a value of ca. −1.1 × 10^9 V/m was determined for ΔE = −0.45 V (Figure 8). Thus, not only the direction of the electric field but also the magnitude are different compared to MHA on Ag, for which a field strength of 2.0 × 10^9 V/m was estimated previously.[69]

Previous studies of the heme protein cytochrome c immobilized on carboxyl-terminated SAMs on Ag electrodes have shown that local electric fields at such thin SAM coatings are sufficiently strong to affect protein structure and dynamics, electron transfer rates and redox potential.[5−8,69,73,75] Comparably large electric fields have also been estimated for interfaces of biological membranes,[4] supporting the view that SAM-coated metal electrodes represent a suitable platform to assess the effects of functionally relevant interfacial electric fields on protein structure and function.

■ CONCLUSIONS

The SEIRA spectroscopic investigation of C5CN and C6CN SAMs on Au electrodes afforded a linear and nonlinear potential-dependence of C≡N band intensities and frequencies, respectively. The linear intensity variations were related to potential-dependent changes of the angle φ between the difference dipole moment and the surface normal, which in turn accounts for the nonlinear potential dependence of the frequencies. The conversion of these frequency changes into a potential-dependent profile of the electric field at the SAM/solution interface relies upon the knowledge of ν and φ at the potential of zero-electric-field (corresponding to $E_{pzc,eff}$), and the difference dipole moment. The determination of each of these quantities via spectroscopic, electrochemical, and theoretical methods is associated with specific uncertainties such that the resultant electric field strengths most likely represent lower limits. Nevertheless, there is a good agreement with predictions from the present electrostatic model which also provides a satisfactory description for nitrile-terminated SAMs on Ag electrodes. Thus, this model seems to be of general applicability for a quick estimate of direction and strength of the interfacial electric field at different electrode/SAM interfaces.

Specific conclusions of this work are the following: (i) The potential-dependent profile of the interfacial electric field as derived from nitrile-terminated SAMs seems to be a good approximation also for carboxyl-terminated SAMs, at least as long as the degree of ionization is small. This may be of particular importance for analyzing electric field effects on biological processes that are frequently probed at electrodes coated by partially charged SAMs. (ii) For the same value of |$E - E_{pzc,eff}$| and SAMs of similar thickness, the modulus of interfacial electric field strengths at SAM-coated Au electrodes is estimated to be lower by a factor of ca. 2 compared to Ag. Due to the different values of $E_{pzc,eff}$, the direction of the

interfacial electric field is opposite for Au and Ag for electrode potentials between ca. 0.0 and −0.6 V, which covers an important part of the potential range for studying interfacial processes of biomolecules. This may account for the different effects on structure and dynamics of biomolecules probed on Au and Ag as discussed previously.[5] (iii) Finally, the present results demonstrate that the electric field strengths at SAM-coated electrodes lie in the range of those predicted for membrane/solution interfaces,[4] such that these electrochemical devices can in fact be considered as simple mimics for biological membranes as far as the electrostatics is concerned.

■ ASSOCIATED CONTENT

⑤ Supporting Information

The Supporting Information is available free of charge on the ACS Publications website at DOI: 10.1021/acs.jpcc.7b08434.

> Additional EIS data for C5CN and C6CN, results of solvatochromism measurements, description of the electrostatic model and its application to Au and Ag electrodes, and analytical data on the synthesized thiol compounds (PDF)

■ AUTHOR INFORMATION

Corresponding Authors
*E-mail: hildebrandt@chem.tu-berlin.de.
*E-mail: jkozuch@stanford.edu.

ORCID ⓘ
Daniel H. Murgida: 0000-0001-5173-0183
Peter Hildebrandt: 0000-0003-1030-5900

Present Addresses
§L.L.: Goethe Universität - Institut für Biophysik, Max-von-Laue-Str. 1, D-60438 Frankfurt, Germany.
‖J.K.: Department of Chemistry, Stanford University, Stanford, California 94305-5012, USA.

Author Contributions
The manuscript was written through contributions of all authors. All authors have given approval to the final version of the manuscript.

Notes
The authors declare no competing financial interest.

■ ACKNOWLEDGMENTS

■ REFERENCES

(1) Sasaki, M.; Takagi, M.; Okamura, Y. A Voltage Sensor−Domain Protein Is a Voltage-Gated Proton Channel. *Science* **2006**, *312*, 589−592.

(2) Catterall, W. A. Structure and Regulation of Voltage-gated Ca^{2+} Channels. *Annu. Rev. Cell Dev. Biol.* **2000**, *16*, 521−555.

(3) Hiller, S.; Garces, R. G.; Malia, T. J.; Orekhov, V. Y.; Colombini, M.; Wagner, G. Solution Structure of the Integral Human Membrane Protein VDAC-1 in Detergent Micelles. *Science* **2008**, *321*, 1206−1210.

(4) Clarke, R. J. The Dipole Potential of Phospholipid Membranes and Methods for its Detection. *Adv. Colloid Interface Sci.* **2001**, *89−90*, 263−281.

(5) Khoa Ly, H.; Wisitruangsakul, N.; Sezer, M.; Feng, J. J.; Kranich, A.; Weidinger, I.; Zebger, I.; Murgida, D. H.; Hildebrandt, P. Electric-Field Effects on the Interfacial Electron Transfer and Protein Dynamics of Cytochrome c. *J. Electroanal. Chem.* **2011**, *660*, 367−376.

(6) Khoa Ly, H.; Sezer, M.; Wisitruangsakul, N.; Feng, J. J.; Kranich, A.; Millo, D.; Weidinger, I. M.; Zebger, I.; Murgida, D. H.; Hildebrandt, P. Surface Enhanced Vibrational Spectroscopies for Probing Transient Interactions of Proteins with Biomimetic Interfaces: Electric Field Effects on Electron Transfer and Protein Dynamics. *FEBS J.* **2011**, *278*, 1382−1390.

(7) Murgida, D. H.; Hildebrandt, P. Disentangling Interfacial Redox Processes of Proteins by SERR Spectroscopy. *Chem. Soc. Rev.* **2008**, *37*, 937−945.

(8) Alvarez-Paggi, D.; Meister, W.; Kuhlmann, U.; Weidinger, I.; Tenger, K.; Zimányi, L.; Rákhely, G.; Hildebrandt, P.; Murgida, D. H. Disentangling Electron Tunneling and Protein Dynamics of Cytochrome c trough a Rationally Designed Surface Mutation. *J. Phys. Chem. B* **2013**, *117*, 6061−6068.

(9) Khan, M. S.; Dosoky, N. S.; Williams, J. D. Engineering Lipid Bilayer Membranes for Protein Studies. *Int. J. Mol. Sci.* **2013**, *14*, 21561−21597.

(10) Tien, H. T. Black Lipid Membranes: Thickness Determination and Molecular Organization by Optical Methods. *J. Theor. Biol.* **1967**, *16*, 97−110.

(11) Stelzle, M.; Weissmüller, G.; Sackmann, E. On the Application of Supported Bilayers as Receptive Layers for Biosensors with Electrical Detection. *J. Phys. Chem.* **1993**, *97*, 2974−2981.

(12) Jeuken, L. J. C.; Connell, S. D.; Nurnabi, M.; O'Reilly, J.; Henderson, P. J. F.; Evans, S. D.; Bushby, R. J. Direct Electrochemical Interaction between a Modified Gold Electrode and a Bacterial Membrane Extract. *Langmuir* **2005**, *21*, 1481−1488.

(13) Harroun, H. T.; Heller, W. T.; Weiss, T. M.; Yang, L.; Huang, H. W. Experimental Evidence for Hydrophobic Matching and Membrane-Mediated Interactions in Lipid Bilayers Containing Gramicidin. *Biophys. J.* **1999**, *76*, 937−945.

(14) Laredo, T.; Dutcher, J. R.; Lipkowski, J. Electric Field Driven Changes of a Gramicidin Containing Lipid Bilayer Supported on a Au(111) Surface. *Langmuir* **2011**, *27*, 10072−10087.

(15) Kozuch, J.; Steinem, C.; Hildebrandt, P.; Millo, D. Combined Electrochemistry and Surface-enhanced Infrared Absorption Spectroscopy of Gramicidin A Incorporated into Tethered Bilayer Lipid Membranes. *Angew. Chem., Int. Ed.* **2012**, *51*, 8114−8117.

(16) Kozuch, J.; Weichbrodt, C.; Millo, D.; Giller, K.; Becker, S.; Hildebrandt, P.; Steinem, C. Voltage-Dependent Structural Changes of the Membrane-Bound Anion Channel hVDAC1 Probed by SEIRA and Electrochemical Impedance Spectroscopy. *Phys. Chem. Chem. Phys.* **2014**, *16*, 9546−9555.

(17) Wiebalck, S.; Kozuch, J.; Forbrig, E.; Tzschucke, C. C.; Jeuken, L. J. C.; Hildebrandt, P. A Novel Tethered Bilayer Lipid Membrane Tailored for the IR Spectroscopic Investigation of Membrane Proteins: Monitoring Catalysis of Cytochrome cbo_3. *J. Phys. Chem. B* **2016**, *120*, 2249−2256.

(18) Jiang, X.; Engelhard, M.; Ataka, K.; Heberle, J. Molecular Impact of the Membrane Potential on the Regulatory Mechanism of Proton Transfer in Sensory Rhodopsin II. *J. Am. Chem. Soc.* **2010**, *132*, 10808−10815.

(19) Ataka, K.; Kottke, T.; Heberle, J. Thinner, Smaller, Faster: IR Techniques To Probe the Functionality of Biological and Biomimetic Systems. *Angew. Chem., Int. Ed.* **2010**, *49*, 5416−5424.

(20) Fried, S. D.; Boxer, S. G. Measuring Electric Fields and Noncovalent Interactions Using the Vibrational Stark Effect. *Acc. Chem. Res.* **2015**, *48*, 998−1006.

(21) Suydam, I. T.; Snow, C. D.; Pande, V. S.; Boxer, S. G. Electric Fields at the Active Site of an Enzyme: Direct Comparison of Experiment with Theory. *Science* **2006**, *313*, 200−204.

(22) Bagchi, S.; Fried, S. D.; Boxer, S. G. A Solvatochromic Model Calibrates Nitriles' Vibrational frequencies to Electrostatic Fields. *J. Am. Chem. Soc.* **2012**, *134*, 10373−10376.

(23) Webb, L. J.; Boxer, S. G. Electrostatic Fields near the Active Site of Human Aldose Reductase: 1. New Inhibitors and Vibrational Stark Effect Measurements. *Biochemistry* **2008**, *47*, 1588−1598.

(24) Fafarman, A. T.; Boxer, S. G. Nitrile Bonds as Infrared Probes of Electrostatics in Ribonuclease S. *J. Phys. Chem. B* **2010**, *114*, 13536−13544.

(25) Fafarman, A. T.; Sigala, P. A.; Schwans, J. P.; Fenn, T. D.; Herschlag, D.; Boxer, S. G. Quantitative, Directional Measurement of Electric Field Heterogeneity in the Active Site of Ketosteroid Isomerase. *Proc. Natl. Acad. Sci. U. S. A.* **2012**, *109*, 299−308.

(26) Fafarman, A. T.; Sigala, P. A.; Herschlag, D.; Boxer, S. G. Decomposition of Vibrational Shifts of Nitriles into Electrostatic and Hydrogen-Bonding Effects. *J. Am. Chem. Soc.* **2010**, *132*, 12811−12813.

(27) Lindquist, B. A.; Furse, K. E.; Corcelli, S. A. Nitrile Groups as Vibrational Probes of Biomolecular Structure and Dynamics: An Overview. *Phys. Chem. Chem. Phys.* **2009**, *11*, 8119−8132.

(28) Fried, S. D.; Bagchi, S.; Boxer, S. G. Extreme Electric Fields Power Catalysis in the Active Site of Ketosteroid Isomerase. *Science* **2014**, *346*, 1510−1514.

(29) Dalosto, S. D.; Vanderkooi, J. M.; Sharp, K. A. Vibrational Stark Effects on Carbonyl, Nitrile, and Nitrosyl Compounds Including Heme Ligands, CO, CN, and NO, Studied with Density Functional Theory. *J. Phys. Chem. B* **2004**, *108*, 6450−6457.

(30) Getahun, Z.; Huang, C.-Y.; Wang, T.; De León, B.; DeGrado, W. F.; Gai, F. Using Nitrile-Derivatized Amino Acids as Infrared Probes of Local Environment. *J. Am. Chem. Soc.* **2003**, *125*, 405−411.

(31) Gai, X. S.; Coutifaris, B. A.; Brewer, S. H.; Fenlon, E. E. A Direct Comparison of Azide and Nitrile Vibrational Probes. *Phys. Chem. Chem. Phys.* **2011**, *13*, 5926−5930.

(32) Hu, W.; Webb, L. J. Direct Measurement of the Membrane Dipole Field in Bicelles Using Vibrational Stark Effect Spectroscopy. *J. Phys. Chem. Lett.* **2011**, *2*, 1925−1930.

(33) Oklejas, V.; Sjostrom, C.; Harris, J. M. SERS Detection of the Vibrational Stark Effect from Nitrile-Terminated SAMs to Probe Electric Fields in the Diffuse Double-Layer. *J. Am. Chem. Soc.* **2002**, *124*, 2408−2409.

(34) Oklejas, V.; Sjostrom, C.; Harris, J. M. Surface-Enhanced Raman Scattering Based Vibrational Stark Effect as a Spatial Probe of Interfacial Electric Fields in the Diffuse Double Layer. *J. Phys. Chem. B* **2003**, *107*, 7788−7794.

(35) Oklejas, V.; Harris, J. M. In-Situ Investigation of Binary-Component Self-Assembled Monolayers: A SERS-Based Spectroelectrochemical Study of the Effects of Monolayer Composition on Interfacial Structure. *Langmuir* **2003**, *19*, 5794−5801.

(36) Kwasnieski, D. T.; Wang, H.; Schultz, Z. D. Alkyl-nitrile Adlayers as Probes of Plasmonically Induced Electric Fields. *Chem. Sci.* **2015**, *6*, 4484−4494.

(37) Schkolnik, G.; Utesch, T.; Salewski, J.; Tenger, K.; Millo, D.; Kranich, A.; Zebger, I.; Schulz, C.; Zimányi, L.; Rákhely, G.; et al. Mapping Local Electric Fields in Proteins at Biomimetic Interfaces. *Chem. Commun.* **2012**, *48*, 70−72.

(38) Völler, J.; Biava, H.; Koksch, B.; Hildebrandt, P.; Budisa, N. Orthogonal Translation Meets Electron Transfer: In Vivo Labeling of Cytochrome C for Probing Local Electric Fields. *ChemBioChem* **2015**, *16*, 742−745.

(39) Miyake, H.; Ye, S.; Osawa, M. Electroless Deposition of Gold Thin Films on Silicon for Surface-Enhanced Infrared Spectroelectrochemistry. *Electrochem. Commun.* **2002**, *4*, 973−977.

(40) Widrig, C. A.; Alves, C. A.; Porter, M. D. Scanning Tunneling Microscopy of Ethanethiolate and n-Octadecanethiolate Monolayers Spontaneously Absorbed at Gold Surfaces. *J. Am. Chem. Soc.* **1991**, *113*, 2805−2810.

(41) Bizzarri, A. R.; Costantini, G.; Cannistraro, S. MD Simulation of a Plastocyanin Mutant Adsorbed onto a Gold Surface. *Biophys. Chem.* **2003**, *106*, 111−123.

(42) Feller, S. E.; Gawrisch, K.; MacKerell, A. D. Polyunsaturated Fatty Acids in Lipid Bilayers: Intrinsic and Environmental Contributions to Their Unique Physical Properties. *J. Am. Chem. Soc.* **2002**, *124*, 318−326.

(43) Vanommeslaeghe, K.; Hatcher, E.; Acharya, C.; Kundu, S.; Zhong, S.; Shim, J.; Darian, E.; Guvench, O.; Lopes, P.; Vorobyov, I.;

et al. CHARMM general force field: A Force Field for Drug-like Molecules Compatible with the CHARMM All-atom Additive Biological Force Fields. *J. Comput. Chem.* **2010**, *31*, 671−690.

(44) Jorgensen, W. L.; Chandrasekhar, J.; Madura, J. D.; Impey, R. W.; Klein, M. L. Comparison of Simple Potential Functions for Simulating Liquid Water. *J. Chem. Phys.* **1983**, *79*, 926−935.

(45) Phillips, J. C.; Braun, R.; Wang, W.; Gumbart, J.; Tajkhorshid, E.; Villa, E.; Chipot, C.; Skeel, R. D.; Kalé, L.; Schulten, K. Scalable Molecular Dynamics with NAMD. *J. Comput. Chem.* **2005**, *26*, 1781−1802.

(46) Feller, S. E.; Gawrisch, K.; MacKerell, A. D. Polyunsaturated Fatty Acids in Lipid Bilayers: Intrinsic and Environmental Contributions to Their Unique Physical Properties. *J. Am. Chem. Soc.* **2002**, *124*, 318−326.

(47) Darden, T.; York, D.; Pedersen, L. Particle mesh Ewald: An N log(N) Method for Ewald Sums in Large Systems. *J. Chem. Phys.* **1993**, *98*, 10089−10092.

(48) van Gunsteren, W. F.; Berendsen, H. J. C. Algorithms for Macromolecular Dynamics and Constraint Dynamics. *Mol. Phys.* **1977**, *34*, 1311−1327.

(49) Humphrey, W.; Dalke, A.; Schulten, K. VMD: Visual Molecular Dynamics. *J. Mol. Graphics* **1996**, *14*, 33−38.

(50) Jeuken, L. J. C.; Daskalakis, N. N.; Han, X.; Sheikh, K.; Erbe, A.; Bushby, R. J.; Evans, S. D. Phase Separation in Mixed Self-assembled Monolayers and its Effect on Biomimetic Membranes. *Sens. Actuators, B* **2007**, *124*, 501−509.

(51) Tlili, A.; Abdelghani, A.; Hleli, S.; Maaref, M. A. Electrical Characterization of a Thiol SAM on Gold as a First Step for the Fabrication of Immunosensors Based on a Quartz Crystal Microbalance. *Sensors* **2004**, *4*, 105−114.

(52) Agonafer, D. D.; Chainani, E.; Oruc, M. E.; Lee, K. S.; Shannon, M. A. Study of Insulating Properties of Alkanethiol Self-Assembled Monolayers Formed Under Prolonged Incubation Using Electrochemical Impedance Spectroscopy. *J. Nanotechnol. Eng. Med.* **2012**, *3*, 031006.

(53) Aschaffenburg, D. J.; Moog, R. S. Probing Hydrogen Bonding Environments: Solvatochromic Effects on the CN Vibration of Benzonitrile. *J. Phys. Chem. B* **2009**, *113*, 12736−12743.

(54) Schkolnik, G.; Salewski, J.; Millo, D.; Zebger, I.; Franzen, S.; Hildebrandt, P. Vibrational Stark Effect of the Electric-field Reporter 4-Mercaptobenzonitrile as a Tool for Investigating Electrostatics at Electrode/SAM/Solution Interfaces. *Int. J. Mol. Sci.* **2012**, *13*, 7466−7482.

(55) Zhang, W.; Markiewicz, B. N.; Doerksen, R. S.; Smith, A. B., III; Gai, F. C≡N Stretching Vibration of 5-Cyanotryptophan as an Infrared Probe of Protein Local Environment: What Determines its Frequency? *Phys. Chem. Chem. Phys.* **2016**, *18*, 7027−7034.

(56) Becka, A. M.; Miller, C. J. Electrochemistry at Hydroxy Thiol Coated Electrodes. 4. Comparison of the Double Layer at Hydroxy Thiol and Alkanethiol Monolayer Coated Au Electrodes. *J. Phys. Chem.* **1993**, *97*, 6233−6239.

(57) Trasatti, S. Work Function, Electronegativity, and Electrochemical Behaviour of Metals. *J. Electroanal. Chem. Interfacial Electrochem.* **1971**, *33*, 351−378.

(58) Ramírez, P.; Andreu, R.; Cuesta, A.; Calzado, C. J.; Calvente, J. J. Determination of the Potential of Zero Charge of Au(111) Modified with Thiol Monolayers. *Anal. Chem.* **2007**, *79*, 6473−6479.

(59) Wang, L.; Rangger, G. M.; Romaner, L.; Heimel, G.; Bučko, T.; Ma, Z.; Li, Q.; Shuai, Z.; Zojer, E. Electronic Structure of Self-assembled Monolayers on Au(111) Surfaces: The Impact of Backbone Polarizability. *Adv. Funct. Mater.* **2009**, *19*, 3766−3775.

(60) Heimel, G.; Romaner, L.; Zojer, E.; Bredas, J. L. The Interface Energetics of Self-Assembled Monolayers on Metals. *Acc. Chem. Res.* **2008**, *41*, 721−729.

(61) Osawa, M.; Ataka, K.; Yoshii, K.; Nishikawa, Y. Surface-Enhanced Infrared Spectroscopy: The Origin of the Absorption Enhancement and Band Selection Rule in the Infrared Spectra of Molecules Adsorbed on Fine Metal Particles. *Appl. Spectrosc.* **1993**, *47*, 1497−1502.

(62) Sondag-Huethorst, J. A. M.; Fokkink, L. G. J. Electrochemical Characterization of Functionalized Alkanethiol Monolayers on Gold. *Langmuir* **1995**, *11*, 2237−2241.

(63) Jeuken, L. J. C. AFM Study on the Electric-Field Effects on Supported Bilayer Lipid Membranes. *Biophys. J.* **2008**, *94*, 4711−4717.

(64) Andrews, S. S.; Boxer, S. G. Vibrational Stark Effects of Nitriles I. Methods and Experimental Results. *J. Phys. Chem. A* **2000**, *104*, 11853−11863.

(65) Schneider, S. H.; Boxer, S. G. Vibrational Stark Effects of Carbonyl Probes Applied to Reinterpret IR and Raman Data for Enzyme Inhibitors in Terms of Electric Fields at the Active Site. *J. Phys. Chem. B* **2016**, *120*, 9672−9684.

(66) Boxer, S. G. Stark Realities. *J. Phys. Chem. B* **2009**, *113*, 2972−2983.

(67) Ringer, A. L.; MacKerell, A. D., Jr. Calculation of the Vibrational Stark Effect Using a First-Principles Quantum Mechanical/Molecular Mechanical Approach. *J. Phys. Chem. Lett.* **2011**, *2*, 553−556.

(68) Smith, C. P.; White, H. S. Theory of the Interfacial Potential Distribution and Reversible Voltammetric Response of Electrodes Coated with Electroactive Molecular Films. *Anal. Chem.* **1992**, *64*, 2398−2405.

(69) Murgida, D. H.; Hildebrandt, P. The Heterogeneous Electron Transfer of Cytochrome c Adsorbed on Coated Silver Electrodes. Electric Field Effects on Structure and Redox Potential. *J. Phys. Chem. B* **2001**, *105*, 1578−1586.

(70) Valette, G. Hydrophilicity of Metal Surfaces, Silver, Gold and Copper Electrodes. *J. Electroanal. Chem. Interfacial Electrochem.* **1982**, *139*, 285−301.

(71) Love, J. C.; Estroff, L. A.; Kriebel, J. K.; Nuzzo, R. G.; Whitesides, G. M. Self-Assembled Monolayers of Thiolates on Metals as a Form of Nanotechnology. *Chem. Rev.* **2005**, *105*, 1103−1170.

(72) Marr, J. M.; Schultz, Z. D. Imaging Electric Fields in SERS and TERS Using the Vibrational Stark Effect. *J. Phys. Chem. Lett.* **2013**, *4*, 3268−3272.

(73) Murgida, D. H.; Hildebrandt, P. Redox and Redox-coupled Processes of Heme Proteins and Enzymes at Electrochemical Interfaces. *Phys. Chem. Chem. Phys.* **2005**, *7*, 3773−3784.

(74) Nölla, T.; Nöll, G. Strategies for "Wiring" Redox-active Proteins to Electrodes and Applications in Biosensors, Biofuel Cells, and Nanotechnology. *Chem. Soc. Rev.* **2011**, *40*, 3564−3576.

(75) Feng, J. J.; Murgida, D. H.; Kuhlmann, U.; Utesch, T.; Mroginski, M. A.; Hildebrandt, P.; Weidinger, I. Gated Electron Transfer of Yeast Iso-1 Cytochrome *c* on SAM-coated Electrodes. *J. Phys. Chem. B* **2008**, *112*, 15202−15211.